

# TOWARDS HARD AND SOFT SHADOW REMOVAL VIA DUAL-BRANCH SEPARATION NETWORK AND VISION TRANSFORMER

Jiajia Liang<sup>1</sup>, Bowen Zhang<sup>1</sup>, Jinwen Deng<sup>1</sup>, Patrick Chan<sup>1\*</sup>

<sup>1</sup>South China University of Technology, scut.edu.cn

202164020270@mail.scut.edu.cn, 202164690534@mail.scut.edu.cn, jingwen\_deng@foxmail.com,  
patrickchan@scut.edu.cn

## Abstract:

Image shadow removal is a crucial task in computer vision. In real-world scenes, shadows alter image color and brightness, posing challenges for perception and texture recognition. Traditional and deep learning methods often overlook the distinct needs for handling hard and soft shadows, thereby lacking detailed processing to specifically address each type of shadow in images. We propose a dual-path model that processes these shadows separately using specially designed loss functions to accomplish the hard and soft shadow removal. The model classifies shadow types and processes them through appropriate paths to produce shadow-free outputs, integrating a Vision Transformer with UNet++ for enhanced edge detail and feature fusion. Our model outperforms state-of-the-art methods and achieves 2.905 RMSE value on the ISTD dataset, which demonstrates greater effectiveness than typical single-path approaches.

## Keywords:

Hard shadow and soft shadow; Dual-path; Transformer; UNet++

## 1. Introduction

Image shadow removal has been a fundamental research topic in the field of computer vision for years. In real-world scenes, on one hand, the shadows cast by objects can change the chromaticity and brightness of certain areas in an image. On the other hand, shadows can affect the texture of certain areas in an image, which poses certain challenges for chromaticity perception and texture recognition. Therefore, removing shadows is pivotal in the domain of computer vision such as object detection and recognition[47], image segmentation[48], target tracking[49], and scene understanding[50].

In recent years, deep learning methods have significantly advanced the field of image shadow removal[1, 2, 3], particularly in dealing with hard shadows, which are characterized by distinct, sharp edges that facilitate boundary identification and shadow masking, while soft shadows are characterized by more diffuse edges that blend into their surroundings, making them less distinct and more challenging to detect accurately. The main challenge with hard shadows lies in the natural restoration of chromaticity

and texture at the shadow edges, where the entire shadow

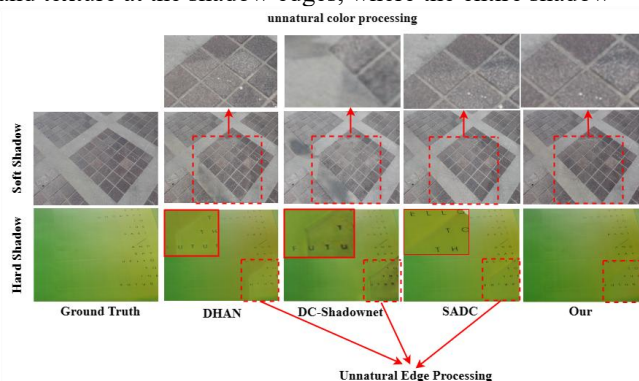


FIGURE 1. Current technology processes results

mask area tends to have more uniform chromaticity and brightness. This allows for reliance on local information over global cues in shadow removal tasks.

Recently, some models have shown excellent performance in the domain of shadow removal, such as G2R-ShadowNet [23], TC-SHADOWGAN [40], and DC-ShadowNet [13]. These methods typically treat hard and soft shadows uniformly, applying the same technique to both types of shadows. This approach overlooks the distinct challenges presented in the removal of hard versus soft shadows. For instance, RYO ABIKO and colleagues enhanced their method's loss function with a Gaussian filter to specifically target loss at shadow edges, aiming to improve shadow removal outcomes [9]. However, this design might be more suitable for handling hard shadows, as they have clearer edges. For soft shadows, which have more blurred edges, the effectiveness of such an approach is limited. Hence, although these methods have demonstrated good performance on datasets predominantly featuring hard shadows, like ISTD [41] and SRD [42], their performance on datasets focused on soft shadows, such as LRSS [43], is not as compelling. This uncovers an important research direction—there is a need to develop advanced methods capable of finely distinguishing and effectively handling both hard and soft shadows, to enhance the application of shadow removal techniques across various scenarios.

To address the challenges faced by traditional shadow

removal techniques in dealing with both soft and hard shadows, we have designed a novel mechanism that can distinguish and separately process soft and hard shadows. In our proposed model, the generator is designed to include two dedicated paths: one focusing on the processing of hard shadows and the other targeting soft shadows. Each path employs specially designed loss functions for independent training, ensuring optimized treatment for different types of shadows.

During the shadow removal process, first, the shadow image is fed into a classifier, which is responsible for determining and outputting the likelihood of the image being a hard or soft shadow. Subsequently, the image is processed through both specialized paths to generate two potential shadow-removed results. Finally, based on the output of the classifier, we merge these two results into the final output image using certain fusion parameters. This strategy not only allows for differentiated treatment based on the softness or hardness of the shadows, thereby reducing errors that may arise from using a single processing method, but it can also effectively handle images that lie in the ambiguous zone between soft and hard shadows, ensuring that various types of shadows can be effectively removed.

The main contributions of this study are summarized more concisely as follows:

(1) We propose a novel mechanism for treating soft and hard shadows differently through parallel processing paths, this method can enhance the ability of our model to distinguish between soft and hard shadow removal in complex scenes.

(2) To the best of our knowledge, this is the first report on integrating Vision Transformer with UNet++ for shadow removal, this combination can boost detail processing capabilities, especially around shadow edges, through a multi-layer feature fusion mechanism.

(3) We carry out comprehensive experiments and ablative analysis on the ISTD dataset, our method surpasses the performance of existing top-performing models demonstrating the efficacy of our proposed method.

## Related Works

Traditional physical methods for image shadow removal primarily rely on in-depth analysis of lighting models, shadow colors, and scene geometry, aiming to simulate and eliminate shadow effects in images [3, 4, 5, 6, 7]. However, these methods exhibit clear limitations, including strong dependence on environmental lighting conditions and scene geometry, as well as insufficient adaptability when faced with complex and variable real-world scenes. Moreover, the accuracy and robustness of such approaches are also limited

when encountering shadows of different types and depths. In contrast to these traditional methods, our proposed approach is capable of effectively handling various types of shadows, achieving efficient and accurate shadow removal effects for both hard and soft shadows.

In the last few years, there has been notable achievement in deep learning methods for the task of image shadow removal. For example, Le et al. [8] and others proposed a new method combining linear illumination transformations and deep learning, which effectively removes shadows from a single image by predicting shadow parameters and shadow masks, significantly improving the accuracy and quality of shadow removal. Similarly, RYO [9] and others developed a new model named CANet, which integrates shadow detection and shadow removal networks, and introduces a ColorBlock structure and trains through an extended dataset, achieving high-precision shadow removal. Furthermore, methods using Generative Adversarial Networks (GAN) have also been applied to shadow removal, where RIS-GAN [10] framework, by exploring residual and illumination information in the shadow removal process, combines rough shadow-free images, estimated negative residual images, and inverse illumination maps to generate detailed shadow-free images. Cun et al. [11] proposed DHAN and SMGAN as well as ST-CGAN [12] further refined the task of shadow removal. However, despite these models making progress in dealing with different types of shadows, their generalization ability remains limited. In contrast, our model can differentiate based on the softness and hardness of shadows, significantly reducing errors that might be introduced by relying on a single processing strategy.

Compared to our method, DC-ShadowNet [13] adopts a similar approach. They designed a network guided by unsupervised learning and a domain classifier, specifically aimed at removing hard and soft shadows from single images. Unlike traditional techniques, DC-ShadowNet innovates by utilizing novel unsupervised loss functions such as physics-based shadow-free chromaticity, shadow-robust perceptual features, and boundary smoothness loss, combined with a domain classifier to guide the generator and discriminator to focus on shadow areas. However, this method does not significantly distinguish between hard and soft shadows but attempts to handle all types of shadows by incorporating traditional physical shadow removal methods into its loss function. Our method, on the other hand, employs two parallel paths trained for diverse shadow profiles in images. Through this differentiated treatment, our model can more effectively adapt to different types of shadow images, thereby enhancing the performance and applicability of shadow removal

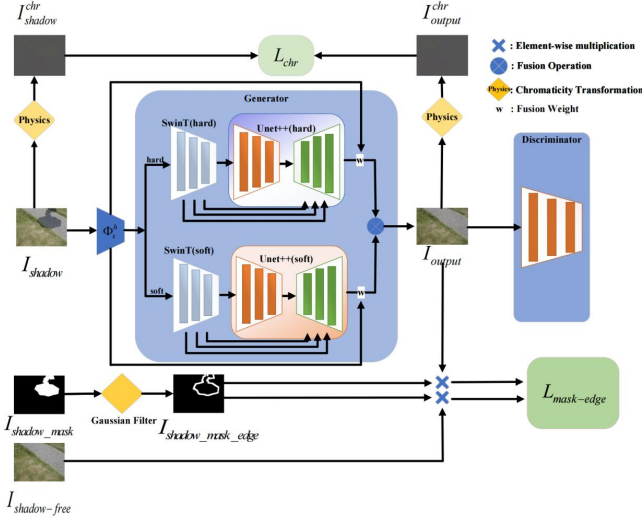


FIGURE 2. General structure of our method

Our approach classifies shadow images into *hard shadows* and *soft shadows*. The shadow removal network is comprised of three components: a classifier  $\Phi_s^h$ , a generator, and a discriminator. The generator includes two pathways, each containing a Swin\_Transformer and a UNet++ with distinct parameters. Each UNet++ encompasses an encoder and a decoder. For the input shadow image  $I_{shadow}$ , the corresponding outputs for shadow-free, shadow mask, shadow-free chromaticity, output chromaticity images and shadow edge mask are denoted as  $I_{output}$ ,  $I_{shadow\_mask}$ ,  $I_{shadow}^{chr}$ ,  $I_{output}^{chr}$ , and  $I_{shadow\_mask\_edge}$  respectively. The classifier  $\Phi_s^h$  is used to generate fusion weight ratios that are then used to combine the outputs of two separate processing pipelines: one for hard shadows and another for soft shadows. To guide the training of our generator and discriminator, we employ unique loss functions for different pipelines. For the soft pipeline, we introduce a shadow-free chromaticity loss function calculated by physical methods from the original shadow image  $I_{shadow}$  and the output shadow-free image  $I_{output}$ . For the hard pipeline, we implement a shadow edge loss  $L_{mask\_edge}$  function derived from the shadow mask using a Gaussian filter.

## 2. Proposed Methods

As is shown in Figure 2, our approach classifies shadow images into hard shadows and soft shadows. The shadow removal network is comprised of three components: a

classifier  $\Phi_s^h$ , a generator, and a discriminator. The generator includes two pathways, each containing a Swin\_Transformer and a UNet++ with distinct parameters. Each UNet++ encompasses an encoder and a decoder. For the input shadow image  $I_{shadow}$ , the corresponding outputs for shadow-free, shadow mask, shadow-free chromaticity, shadow chromaticity and shadow edge mask are denoted as  $I_{output}$ ,  $I_{shadow\_mask}$ ,  $I_{shadow}^{chr}$ ,  $I_{output}^{chr}$ , and  $I_{shadow\_mask\_edge}$  respectively. The classifier  $\Phi_s^h$  is used to generate fusion weight ratios that are then used to combine the outputs of two separate processing pipelines: one for hard shadows and another for soft shadows. To guide the training of our generator and discriminator, we employ unique loss functions for different pipelines. For the soft pipeline, we introduce a shadow-free chromaticity loss  $L_{chr}$  function calculated by physical methods from the original shadow image  $I_{shadow}$  and the output shadow-free image  $I_{output}$ . For the hard pipeline, we implement a shadow edge loss function derived from the shadow mask using a Gaussian filter.

Given a shadow image ( $I_{shadow}$ ), a pre-trained classification network decouples the type of shadow into a hard shadow or soft shadow later processing. The classifier outputs a binary probability distribution,  $[P_{hard}, P_{soft}]$ , indicating the likelihood of the image  $I_{shadow}$  which category it belonged in. Subsequently, the image is concurrently propagated along two distinct pipelines: one for hard shadows and another for soft shadows. Within each pipeline, a Transformer architecture extracts a hierarchical feature maps of the image, which is subsequently inputted into a U-Net model. The outputs of the two pathways, each representing a potential shadow-free image, are then integrated through a fusion layer. This layer weights the outputs based on the initial probability assessments  $[P_{hard}, P_{soft}]$  provided by the classifier.

The created shadow-free image  $I_{output}$  is then paired with a real shadow-free image  $I_{shadow\_free}$  and put into a discriminator. The objective of discriminator is to distinguish between generated images  $I_{output}$  and genuine shadow-free images  $I_{shadow\_free}$ .

To meet the distinct needs of eliminating hard and soft shadows, we incorporated additional loss functions beyond the standard ones such as adversarial loss, similarity loss, and perceptual loss. Specifically, we introduced two tailored loss functions to refine the training for each shadow type. For the soft shadow path, a chromaticity loss function calculates the

difference in color characteristics between the input shadow image's shadow-free chromaticity and the output shadow-free image. For the hard shadow path, a shadow mask edge loss function is employed to emphasize the precision at the shadow boundaries during loss computation.

### 3.1 Multi-feature fusion structure

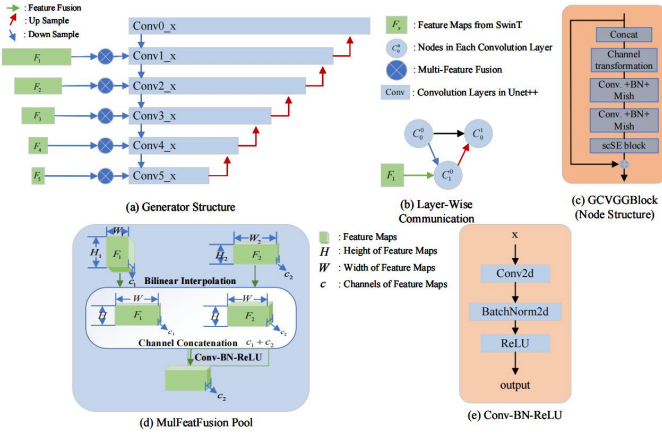


FIGURE 3. Overview of the proposed multi-scale fusion network

Figure 3 outlines the architecture of a complex multi-scale fusion network designed for processing feature maps extracted from an input source. The network is composed of several key components: The network integrates multiple convolutional layers with upsampling and downsampling strategies (a), facilitating feature fusion at various scales. Layer-wise communication (b) is depicted to enhance feature map flow, while the GCVGG block (c) shows the detailed processing within each node. The Multi-FeatFusion Pool (d) emphasizes the combination of feature maps through bilinear interpolation and channel concatenation. Finally, a basic convolutional operation sequence is shown in (e), outlining the processing steps for each input. This architecture aims to leverage multi-scale information for improved image analysis.

The architecture of the generators is segmented into three main components: the feature extractor, the encoder-decoder, and the multi-feature fusion module. The feature extractor utilizes the Swin-Transformer [14], an effective framework that employs hierarchical representation alongside shifted window-based self-attention for feature extraction. This method allows the Swin-Transformer to identify intricate patterns across multiple scales, vital for tasks that demand intricate spatial analysis and the integration of features from various network levels. Following extraction, four feature maps undergo integration within different

decoder stages through a multi-feature fusion module, fostering efficient feature combinations throughout the network.

The MulFeatFusion\_pool module plays a pivotal role in merging features from different network levels. It processes two unique feature maps, employing Bilinear Interpolation to align their spatial dimensions before concatenation along the channel dimension. Subsequently, this concatenated output is processed through a specific convolutional layer called Conv-BN-ReLU that includes batch normalization and ReLU activation, compressing the channel count of the fused feature map for consistent integration with the decoder, the formula for the convolution layer can be expressed as:

$$o = \delta(N(Conv(x))) \quad (1)$$

In the equation, represents for a 2D convolution layer extracting features, denotes a batch normalization layer for stabilizing outputs and the ReLU activation function introduces non-linearity, resulting in the final output. Thus, enhancing feature fusion which is critical for the model's reconstruction or prediction capabilities.

For the encoding and decoding apparatus within the generators, charged with the task of shadow removal, the framework is predicated on the UNet++ [15] model. This structure, detailed in Figure 2(a), is composed of a descending series of convolution nodes across five layers, with node counts reducing from six to one from conv0\_x to conv5\_x. Each node's architecture, as depicted in Figure 2(c), is constituted of a residual block featuring convolutional layers, batch normalization layers [16], Mish activation functions [17], and scSE blocks [18]. The information flow within each node, as elucidated in Figure 2(b), is characterized by the primordial node of each layer acquiring downsampled data from the antecedent layer's node, amalgamating it with the incoming feature map, and subsequently elevating this data through upsampling to successive nodes within the same and subsequent layers. Nodes not situated at the commencement of their respective layers do not assimilate external feature map inputs.

### 3.2 Shadow Chromaticity Loss

Soft shadows are commonly influenced by complex lighting conditions, such as the direction, intensity, and color of light. These changes can cause variations in color and brightness in shadow areas, especially in the transition areas between shadow and non-shadow regions, which often exhibit extensive chromaticity transitions. To restore these transition areas more accurately, we focus on achieving chromaticity consistency between shadow and non-shadow images. For this purpose, in training the generator for soft shadow paths, we have incorporated Shadow Chromaticity

Loss [19]. The Shadow Chromaticity Loss function is designed for shadow removal in images, comprising two main steps: entropy minimization [20] and illumination compensation [21]. Initially, the values of the RGB channels are normalized:

$$[X', Y', Z'] = R / (X + Y + Z), R \in [X, Y, Z] \quad (2)$$

Here, X, Y, Z represent the values of the three channels, and then the input image with shadows is mapped to the logarithmic chromaticity space.

$$[\rho_1, \rho_2, \rho_3] = [\log(X'), \log(Y'), \log(Z')] \quad (3)$$

Then, for each  $\theta$  value from 1 to 180 degree, the two-dimensional log chromaticity image is projected onto a one-dimensional space. The entropy of each projection is calculated, and the projection direction with the minimum entropy is selected as the optimal direction. Using this direction, a shadow-free chromaticity image is generated, but there may be a color shift due to the projection process. Then, by selecting the brightest set of pixels from the input image, the colors in the chromaticity image are adjusted to compensate for this color shift, resulting in a chromaticity image that reflects the original lighting colors of the non-shadowed regions. Finally, a physically-based shadow-free chromaticity image is used to guide the shadow removal generator through a chromaticity loss function, ensuring that the chromaticity of the output image is similar to that of the shadow-free chromaticity image, thereby achieving a consistent chromaticity effect.

### 3.3 Shadow Mask Edge Loss

Hard shadows have clear boundaries, and during the process of shadow removal, these edges often form a stark contrast with the non-shadowed areas. To ensure that the texture and color at the edges of the shadows can be realistically restored, we specifically introduce a shadow mask edge loss in training the generator for hard shadow paths. The purpose of this is to focus on the boundary between the shadowed and non-shadowed areas. We combine the Gaussian and Sobel filters to produce a shadow boundary mask that emphasizes these edges.

$$M_{edge} = \begin{cases} 1 & G(Edge(M_{gt})) > 0 \\ 0 & \text{otherwise,} \end{cases} \quad (4)$$

In this equation,  $G$  stands for Gaussian filter.

The difference between the real image  $I_g$  and the generated shadow-free image  $I_{output}$  is calculated using  $M_{edge}$ , and the element-wise product of these differences is computed. Then, the L2 norm (i.e., the Euclidean distance) of the product results is calculated, summing over all pixel

positions  $i$  to obtain the shadow edge loss function. This process helps to more accurately handle the shadow edges, generating images that look more natural and without obvious shadows. The corresponding calculation formula is as follows:

$$L_{edge} = \sum_i^N \left\| (I_{gt} - I_{output}) \bullet M_{edge} \right\| \quad (5)$$

## 4. Experiments

To validate our approach, we conducted experiments on the ISTD dataset[41], LRSS dataset[43], and the expanded LRSS dataset, evaluating the effectiveness of our method using RMSE[51], PSNR[52], and SSIM[52] metrics. The equipment utilized was a V100-32GB, and the experiments were performed on a platform with CUDA 11.8, using Python 3.8 as our programming language and PyTorch 2.0.0 as our deep learning framework.

### 4.1 Experimental details

**Datasets:** We used the ISTD[41] and LRSS datasets[43], along with an expanded version of the LRSS dataset. The ISTD dataset consists of 1,330 training tuples and 540 testing tuples, each tuple containing shadow images, shadow masks, and shadow-free images. This dataset predominantly features hard shadows, constituting about 70%-80% of the images. The LRSS dataset, originally very small and focused on soft shadows, includes only 34 image groups each with shadow images, shadow masks, and shadow-free images, sourced from the work of Yeying Jin[23]. Given the limited size of the LRSS dataset, we expanded it using the MaskGAN[24] methodology to generate additional training data. This expansion was aimed at enhancing the dataset's robustness and improving the model's training efficacy.

**Evaluation Metrics:** To gauge the effectiveness of our shadow removal model, we utilized four established metrics:

(1) RMSE: Reflects the average magnitude of the error between the predicted and the true images. Lower RMSE values indicate better performance.

$$RMSE(I, K) = \sqrt{\frac{1}{MN} \sum_{i=1}^M \sum_{j=1}^N (I(i, j) - K(i, j))^2} \quad (6)$$

Where  $I(i, j)$  and  $K(i, j)$  are the pixel values at position in images I and K, respectively.

M and N are the number of rows and columns in the images, respectively.

(2) MSE: Measures the average squared differences between the reconstructed and the original images. Lower MSE values denote higher accuracy.

(3) PSNR: Assesses image reconstruction quality, with higher values suggesting a better-quality reconstruction.

$$PSNR = 20 \cdot \log_{10} \left( \frac{MAX_I}{\sqrt{MSE}} \right) \quad (7)$$

$MAX_I$  represents the maximum possible pixel value of the image.

(4) SSIM: Evaluates the perceived change in image structure, brightness, and contrast. Higher SSIM values imply better image quality.

$$SSIM(x, y) = \frac{(2u_x u_y + c_1)(2\sigma_{xy} + c_2)}{(u_x^2 + u_y^2 + c_1)(\sigma_x^2 + \sigma_y^2 + c_2)} \quad (8)$$

Pixel values of windows:  $\mu_x$  &  $\mu_y$

Variations:  $\sigma_x^2$  &  $\sigma_y^2$

Covariance:  $\sigma_{xy}$

Division with Weak Denominator:  $c_1 = (k_1 L)^2$ ,

$c_2 = (k_2 L)^2$  with L representing the dynamic range of the pixel-values and  $k_1=0.01$  and  $k_2=0.03$  by default.

$$SSIM(X, Y) = \frac{1}{M} \sum_{i=1}^M SSIM(x_i, y_i) \quad (9)$$

M: number of windows in the image

$(x_i, y_i)$ : corresponding windows in X and Y.

These metrics were chosen for their relevance to image quality assessment and their common use in image processing tasks. The relationship between these metrics and model performance is straightforward: better models yield lower RMSE and MSE, and higher PSNR and SSIM scores.

## 4.2 Comparison to the State of the Art

Our model is evaluated against state-of-the-art (SOTA) models of the past three years, particularly those utilizing GANs, across the ISTD, ISTD+, and SRD datasets. The evaluations are detailed in Tables 1 through 3. We compared Red indicators highlight unnatural color processing in other methods versus the improved performance of our approach. our method with Guo et al. [25], Deshadownet [26], ST-CGAN [27], Mask-ShadowGAN [28], Direction-Aware Spatial Context Feature [29], AngularGAN [30], DHAN [31],

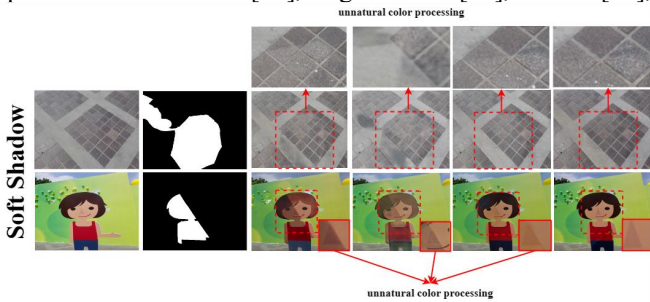


FIGURE 4. Comparison of shadow removal results on soft shadow images

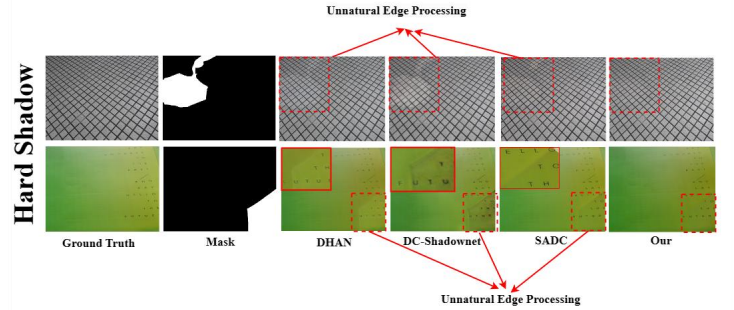


FIGURE 5. Comparison of shadow removal from hard shadow images red boxes and arrows point to areas of unnatural edge processing by different methods, in contrast to the more natural results produced by our method.

RIS-GAN [32], CLA-GAN [33], AEF [34], PULSr [35], DC-ShadowGAN [36], Zhu et al. [37], BMNet [38] and SADC [39].

From the quantitative comparison in Table 1, it can be seen that our model outperforms the current state-of-the-art (SOTA) models on the ISTD dataset: we have the best RMSE values in the shadow areas, non-shadow areas, and overall. For the shadow areas, we also have the best SSIM and PSNR values. Furthermore, as can be seen from Figure 4 and Figure 5, our model demonstrates superior performance on both hard shadow images and soft shadow images: for hard shadow images, our model achieves more natural edge processing of shadows; for soft shadow images, our model allows for more natural color transitions.

## 4.3 Ablation Study

Overview and Objective: In the second section, we first elucidate the key differences between soft and hard shadows, as well as how these distinctions pose unique challenges in the task of shadow removal. Based on this insight, we have developed a method that treats soft and hard shadows separately. Our innovation lies in the dual-path architecture of the generator model, which is optimized to cater to the characteristics of soft and hard shadows respectively. During the training process, we employ a specific combination of loss functions for each path to enhance the model's performance on the corresponding type of shadows. Specifically, when training the soft shadow path, we freeze the hard shadow path and use consistency, adversarial, perceptual, and chromaticity loss functions to train on a dedicated soft shadow dataset. Conversely, when training the hard shadow path, the soft shadow path is frozen, and we apply consistency, adversarial, perceptual, and shadow edge loss functions on a hard shadow dataset. The configuration of our ablation experiment is structured to verify the dual-path

**TABLE 1.** Quantitative comparison with the SOTA methods on the ISTD dataset. Symbol ‘-’ represents values that are not available. The red values indicate the best performances.

Methods	Citation	RMSE			SSIM			PSNR		
		Shad.	No.Shad.	All	Shad.	No.Shad.	All	Shad.	No.Shad.	All
Guo <i>et al.</i> [25]	CVPR/2011	18.65	7.76	9.26	0.964	0.975	0.919	27.76	26.44	23.08
Deshadownet [26]	CVPR/2017	17.96	6.53	8.47						
ST-CGAN [27]	CVPR/2018	10.11	5.76	6.47	0.981	0.959	0.932	33.93	30.18	27.90
Mask-ShadowGAN [28]	ICCV/2019	10.57	5.91	6.67	0.980	0.959	0.928	31.73	29.02	26.36
DSC [29]	CVPR/2018	8.45	5.03	5.59	0.984	0.969	0.944	34.64	31.26	29.00
AngularGAN [30]	CVPRW/2019	9.78	7.67	8.16						
DHAN [31]	AAAI/2020	7.49	5.30	5.66	0.988	0.971	0.954	35.53	31.05	29.11
RIS-GAN [32]	AAAI/2020	8.99	6.33	6.95	-	-	-	-	-	-
CLA-GAN [33]	PG/2020	9.01	6.25	6.62	-	-	-	-	-	-
AEF [34]	CVPR/2021	7.98	5.54	5.94	0.974	0.880	0.844	34.39	28.61	27.11
PULSr [35]	CVPR/2021	6.98	4.94	5.12	-	-	-	32.65	34.71	<b>34.45</b>
DC-ShadowGAN [36]	CVPR/2022	10.55	5.79	6.57	0.976	0.958	0.922	31.69	28.99	26.38
Zhu <i>et al.</i> [37]	AAAI/2022	7.44	3.74	4.79	0.980	<b>0.982</b>	0.952	34.94	<b>35.58</b>	31.72
BMNet [38]	CVPR/2022	7.60	4.59	5.02	0.988	0.976	0.959	35.61	32.80	30.28
ShadowFormer[44]	CVPR/2023	6.16	3.90	4.27	-	-	-	-	-	-
SADC [39]	2024	7.19	5.06	5.41	<b>0.989</b>	0.976	<b>0.961</b>	35.52	31.97	29.85
Our Model	-	<b>6.29</b>	<b>5.64</b>	<b>3.35</b>	<b>0.989</b>	0.965	0.950	<b>35.92</b>	30.04	28.57

design's role in augmenting the model's effectiveness, while also precisely illustrating how our approach independently processes both soft and hard shadows.

**Design:** As described in section three of this document, our generator is designed to include two paths: a hard shadow path and a soft shadow path, each equipped with a Swin-Transformer for feature extraction and connected to a UNet++ with multi-layer feature fusion. In the soft shadow path, we utilize consistency, adversarial, perceptual, and chromaticity loss functions for training on a dedicated soft shadow dataset. For the hard shadow path, we apply consistency, adversarial, perceptual, and shadow edge loss functions on a hard shadow dataset. To verify the effectiveness of our method, we have constructed the following control experiment design:

**Control Group:** The dual-path model undergoes its first comprehensive training using consistency, adversarial, and perceptual loss functions on a mixed dataset containing both soft and hard shadows. Subsequently, we train only the hard shadow path, freezing the soft shadow path, and using shadow edge loss function on a dedicated hard shadow dataset. Similarly, when training only the soft shadow path, we freeze the hard shadow path and apply the chromaticity loss function on a soft shadow dataset. Finally, additional training is conducted for the fusion layer of the dual-path model on the mixed dataset while freezing all other layers.

**Experimental Group A:** The single-path model is trained entirely on a specialized hard shadow mixed dataset using consistency, adversarial, and perceptual loss functions.

**Experimental Group B:** The single-path model is trained

entirely on a specialized soft shadow mixed dataset using consistency, adversarial, and perceptual loss functions.

To ensure the rigor of the experiment, the control group and all experimental groups undergo the same number of training epochs. We will detail the results of testing these models on the mixed shadow dataset, the hard-shadow-only dataset, and the soft-shadow-only dataset in the subsequent results section. We anticipate that the dual-path model, optimized with specific loss function combinations for their respective shadow characteristics, will demonstrate superior performance on specific datasets. Specifically, we expect the dual-path model to provide more accurate and refined shadow removal effects compared to the single-path model on dedicated soft and hard shadow datasets.

In alignment with the distinctions between soft and hard shadows outlined in Section 2 and under expert guidance, we meticulously selected images from the ISTD and LRSS datasets to create two distinct sets: one comprising only hard shadow images and the other only soft shadow images. The hard shadow set, primarily sourced from the ISTD dataset, includes images with sharp, well-defined edges. The soft shadow set, derived from the expanded LRSS dataset, features images with diffuse, less defined shadows. Our mixed dataset combines images from both ISTD and the expanded LRSS, containing both types of shadows, ensuring a balanced representation of soft and hard shadows to facilitate comprehensive analysis.

The quantitative performance results of the dual-path model trained on both soft and hard shadow datasets across three datasets: hard dataset, soft dataset, and hard and soft dataset.

According to the data in Tables 2, 3, and 4, our model was trained on both soft and hard shadows and performed better across all three datasets than models trained only on a single type of shadow (either hard or soft shadows). Specifically, the root mean square error (RMSE) of models trained only on hard or soft shadows is higher across all datasets compared to the dual-path model trained on both types of datasets, in shadow regions, non-shadow regions, and overall. A lower RMSE[51] indicates that the model's generated shadow-free images are closer to the original shadow-free images, demonstrating stronger image restoration capabilities. Similarly, the peak signal-to-noise ratio (PSNR) of these single-path models is lower than that of the dual-path model, where a higher PSNR[52] indicates greater accuracy in image restoration. The performance differences in terms of the Structural Similarity Index Measure (SSIM) among the three models are minimal. A higher SSIM[52] value signifies that the processed image is more similar to the original in terms of brightness, contrast, and structural information, thereby having a closer visual appearance to the original.

**TABLE 2.** The quantitative performance results of the single-path model trained only on hard shadows across three datasets('hard' stands for hard dataset, 'hard soft' stands for hard and soft dataset and 'soft' stands for soft dataset. The same as below.)

Model trained solely on the hard shadow dataset (single-path)									
Dat aset	RMSE			SSIM			PSNR		
	Shad	Non.	All	Shad	Non.	All	Shad	Non.	All
hard	7.04	7.44	4.31	0.99	0.97	0.94	34.77	27.77	26.56
hard soft	8.81	9.41	5.47	0.99	0.96	0.94	32.66	26.01	24.60
soft	16.51	13.19	8.30	0.94	0.88	0.82	21.65	21.65	18.15

**TABLE 3.** The quantitative performance results of the single-path model trained only on soft shadows across three datasets

Model trained solely on the soft shadow dataset (single-path)									
Data set	RMSE			SSIM			PSNR		
	Shad	Non.	All	Shad	Non.	All	Shad.	Non.	All
hard	14.26	6.23	4.68	0.99	0.97	0.95	29.33	28.87	25.01
hard soft	14.11	9.72	6.21	0.99	0.97	0.94	29.59	27.67	24.54
soft	19.77	23.29	12.80	0.97	0.90	0.84	25.57	22.95	20.49

**TABLE 3.** The quantitative performance results of the dual-path model trained on both soft and hard shadow datasets across three datasets

Model trained solely on both soft and hard shadow dataset (dual-path)									
Dat aset	RMSE			SSIM			PSNR		
	Shad	Non.	All	Shad	Non.	All	Shad	Non.	All
hard	6.29	5.63	3.34	0.99	0.97	0.96	35.92	30.04	25.01
hard soft	8.16	7.39	4.44	0.99	0.96	0.95	33.54	28.27	24.54
soft	15.85	12.26	7.80	0.95	0.88	0.82	22.03	22.41	20.49

Furthermore, we observed that the dual-path model trained on a mixed dataset performs better on both hard and soft shadow datasets than models trained only on a single type of shadow dataset. This finding suggests that models trained specifically on one type of shadow exhibit limited generalization capabilities. It is important to note that shadows in images often contain elements of both soft and hard shadows, and there is no clear boundary between them; shadow classification should not be seen as a simple binary problem. In practice, some images labeled as soft shadows might exhibit characteristics of hard shadows, and vice versa. Therefore, the dual-path model integrates data from both

types of shadows and, guided by specific functions (such as an edge function for hard shadow edges and a chroma function for soft shadows), learns to handle different shadow features. This approach plays a harmonizing role during model training, allowing the techniques developed for hard shadows to aid in the removal of soft shadows and vice versa. This cross-learning strategy not only enhances the model's flexibility in application but also improves its practicality in complex environments.

## 5. Conclusion

In this study, we introduced a novel image shadow removal method that processes hard and soft shadows separately through a unique dual-path model. This model utilizes a classifier to first identify the type of shadow, then removes it through specially designed pathways, significantly enhancing the accuracy and efficiency of the removal process. The hard shadow path focuses on shadows with clear edges using an edge loss function, while the soft shadow path handles blurred-edge shadows using a chromaticity loss function. Additionally, our model outperformed existing top models on the ISTD dataset, setting a new performance benchmark. Future work will focus on testing and optimizing our model on more datasets to enhance its generalizability and practicality. We believe the results of this research not only advance shadow removal technology but also provide valuable insights for related computer vision applications.

## References

- [1] B. Ding, C. Long, and C. Xiao, "Argan: Attentive recurrent generative adversarial network for shadow detection and removal," in Proc. of the IEEE/CVF International Conference on Computer Vision (ICCV), 2019.
- [2] H. Le and D. Samaras, "Shadow removal via shadow image decomposition," in Proc. of the IEEE/CVF International Conference on Computer Vision (ICCV), 2019, pp. 8578–8587.
- [3] L. Qu, J. Tian, S. He, Y. Tang, and R. W. H. Lau, "Deshadownet: A multi-context embedding deep network for shadow removal," in Proc. of the IEEE Conference on Computer Vision and Pattern Recognition (CVPR), 2017.
- [4] G. D. Finlayson and M. S. Drew, "4-sensor camera calibration for image representation invariant to shading, shadows, lighting, and specularities," in Proc. Eighth IEEE International Conference on Computer Vision (ICCV), vol. 2, pp. 473–480, 2001.
- [5] G. D. Finlayson, M. S. Drew, and C. Lu, "Intrinsic images by entropy minimization," in European Conference on Computer Vision, pp. 582–595, 2004.
- [6] G. D. Finlayson, M. S. Drew, and C. Lu, "Entropy minimization for shadow removal," International Journal of Computer Vision, vol. 85, no. 1, pp. 35–57, 2009.
- [7] G. D. Finlayson, S. D. Hordley, C. Lu, and M. S. Drew, "On the removal of shadows from images," IEEE Transactions on Pattern Analysis and Machine Intelligence, vol. 28, no. 1, pp. 59–68, 2005.
- [8] H. Le and D. Samaras, "Shadow Removal via Shadow Image Decomposition," in Proc. of the 2019 IEEE/CVF International Conference on Computer Vision (ICCV), IEEE, 2019.
- [9] R. Abiko and M. Ikehara, "Channel Attention GAN Trained With Enhanced Dataset for Single-Image Shadow Removal," IEEE Access, vol. 10, 2022, doi: 10.1109/ACCESS.2022.3147063.
- [10] L. Zhang, C. Long, X. Zhang, and C. Xiao, "RIS-GAN: Explore Residual and Illumination with Generative Adversarial Networks for Shadow Removal," in Proc. of the Thirty-Fourth AAAI Conference on Artificial Intelligence (AAAI-20), Wuhan University of Science and Technology; Kitware Inc.; School of Computer Science, Wuhan University, 2020.
- [11] X. Cun, C.-M. Pun, and C. Shi, "Towards Ghost-Free Shadow Removal via Dual Hierarchical Aggregation Network and Shadow Matting GAN," in Proc. of the Thirty-Fourth AAAI Conference on Artificial Intelligence (AAAI-20), University of Macau; Xi'an University of Technology, 2020.
- [12] J. Wang, L. Hui, X. Li, and J. Yang, "Stacked Conditional Generative Adversarial Networks for Jointly Learning Shadow Detection and Shadow Removal," arXiv preprint arXiv:1712.02478, 2017.
- [13] Y. Jin, A. Sharma, and R. T. Tan, "DC-ShadowNet: Single-Image Hard and Soft Shadow Removal Using Unsupervised Domain-Classifer Guided Network," in Proc. of the IEEE/CVF Conference on Computer Vision and Pattern Recognition (CVPR), National University of Singapore; Yale-NUS College, 2022.
- [14] Z. Liu, Y. Lin, Y. Cao, H. Hu, Y. Wei, Z. Zhang, S. Lin, and B. Guo, "Swin Transformer: Hierarchical Vision Transformer using Shifted Windows," arXiv, 2021.
- [15] Z. Zhou, M. M. R. Siddiquee, N. Tajbakhsh, and J. Liang, "UNet++: A nested U-Net architecture for medical image segmentation," in Deep Learning in Medical Image Analysis and Multimodal Learning for Clinical Decision Support, Springer, Cham, Switzerland, 2018, pp. 3–11.

- [16] D. Misra, "Mish: A self regularized non-monotonic activation function," arXiv:1908.08681, 2019.
- [17] S. Ioffe and C. Szegedy, "Batch normalization: Accelerating deep network training by reducing internal covariate shift," in Proc. of the International Conf. on Machine Learning (ICML), 2015, pp. 448–456.
- [18] A. G. Roy, N. Navab, and C. Wachinger, "Concurrent spatial and channel 'squeeze & excitation' in fully convolutional networks," in Proc. of the International Conf. on Medical Image Computing and Computer-Assisted Intervention (MICCAI), 2018, pp. 421–429.
- [19] DC-ShadowNet: Single-Image Hard and Soft Shadow Removal Using Unsupervised Domain-Classifer Guided Network," in Proc. of the IEEE/CVF International Conference on Computer Vision (ICCV), 2022.
- [20] G. D. Finlayson, M. S. Drew, and C. Lu, "Entropy minimization for shadow removal," *International Journal of Computer Vision*, vol. 85, no. 1, pp. 35–57, 2009.
- [21] M. S. Drew, G. D. Finlayson, and S. D. Hordley, "Recovery of chromaticity image free from shadows via illumination invariance," in *IEEE Workshop on Color and Photometric Methods in Computer Vision*, ICCV'03, pp. 32–39, 2003.
- [22] X. Cun, C.-M. Pun, and C. Shi, "Towards Ghost-Free Shadow Removal via Dual Hierarchical Aggregation Network and Shadow Matting GAN," in Proc. AAAI Conf. on Artificial Intelligence, vol. 34, no. 07, pp. 10,680–10,687, 2020.
- [23] Z. Liu, H. Yin, X. Wu, Z. Wu, Y. Mi, and S. Wang, "From Shadow Generation to Shadow Removal," in Proc. of the IEEE/CVF Conference on Computer Vision and Pattern Recognition (CVPR), 2021.
- [24] X. Hu, Y. Jiang, C.-W. Fu, and P.-A. Heng, "Mask-ShadowGAN: Learning to Remove Shadows from Unpaired Data," in Proc. of the IEEE/CVF International Conference on Computer Vision (ICCV), 2019. Available: <https://arxiv.org/abs/1903.10683>
- [25] R. Guo, Q. Dai, and D. Hoiem, "Paired regions for shadow detection and removal," *IEEE Transactions on Pattern Analysis and Machine Intelligence*, vol. 35, no. 12, pp. 2956–2967, 2012.
- [26] L. Qu, J. Tian, S. He, Y. Tang, and R. W. H. Lau, "DeshadowNet: A Multi-context Embedding Deep Network for Shadow Removal," in Proc. IEEE Conf. on Computer Vision and Pattern Recognition (CVPR), 2017.
- [27] J. Wang, X. Li, and J. Yang, "Stacked conditional generative adversarial networks for jointly learning shadow detection and shadow removal," in Proc. of the IEEE Conference on Computer Vision and Pattern Recognition (CVPR), 2018, pp. 1788–1797.
- [28] X. Hu, Y. Jiang, C.-W. Fu, and P.-A. Heng, "Mask-shadowgan: Learning to remove shadows from unpaired data," in Proc. of the IEEE/CVF International Conference on Computer Vision (ICCV), 2019, pp. 2472–2481.
- [29] X. Hu, C.-W. Fu, L. Zhu, J. Qin, and P.-A. Heng, "Direction-aware spatial context features for shadow detection and removal," *IEEE Transactions on Pattern Analysis and Machine Intelligence*, vol. 42, no. 11, pp. 2795–2808, 2019.
- [30] O. Sidorov, "Conditional GANs for Multi-Illuminant Color Constancy: Revolution or Yet Another Approach?" in Proc. IEEE Conf. on Computer Vision and Pattern Recognition (CVPR).
- [31] X. Cun, C.-M. Pun, and C. Shi, "Towards ghost-free shadow removal via dual hierarchical aggregation network and shadow matting gan," in Proc. of the AAAI Conference on Artificial Intelligence, vol. 34, no. 07, pp. 10,680–10,687, 2020.
- [32] L. Zhang, C. Long, X. Zhang, and C. Xiao, "Ris-gan: Explore residual and illumination with generative adversarial networks for shadow removal," in Proc. of the AAAI Conference on Artificial Intelligence, vol. 34, no. 07, pp. 12,829–12,836, 2020.
- [33] L. Zhang, C. Long, Q. Yan, X. Zhang, and C. Xiao, "Cla-gan: A context and lightness aware generative adversarial network for shadow removal," in *Computer Graphics Forum*, vol. 39, no. 7, pp. 483–494, Wiley Online Library, 2020.
- [34] L. Fu, C. Zhou, Q. Guo, F. Juefei-Xu, H. Yu, W. Feng, Y. Liu, and S. Wang, "Auto-exposure fusion for single-image shadow removal," in Proc. of the IEEE/CVF International Conference on Computer Vision, pp. 10,571–10,580, 2021.
- [35] F.-A. Vasluianu, A. Romero, L. Van Gool, and R. Timofte, "Shadow removal with paired and unpaired learning," in Proc. of the IEEE/CVF Conference on Computer Vision and Pattern Recognition, pp. 826–835, 2021.
- [36] Y. Jin, A. Sharma, and R. T. Tan, "DC-ShadowNet: Single-Image Hard and Soft Shadow Removal Using Unsupervised Domain-Classifer Guided Network," in Proc. of the IEEE/CVF International Conference on Computer Vision, pp. 5027–5036, 2021.
- [37] Y. Zhu, Z. Xiao, Y. Fang, X. Fu, Z. Xiong, and Z.-J. Zha, "Efficient Model-Driven Network for Shadow Removal," 2022.
- [38] Y. He, Y. Xing, T. Zhang, and Q. Chen, "Bijective mapping network for shadow removal," in Proc. of the

- IEEE/CVF Conference on Computer Vision and Pattern Recognition, pp. 5627–5636, 2022.
- [39] Y. Xu, M. Lin, H. Yang, K. Li, Y. Shen, F. Chao, and R. Ji, "Shadow-aware dynamic convolution for shadow removal," *Pattern Recognition*, vol. 112, no. 3, pp. 107-115, 2022.
- [40] C. Tan, X. Feng, B. Chen, and J. Long, "TC-SHADOWGAN: A target-consistency generative adversarial network for unpaired shadow removal," in *Proc. IEEE Int. Conf. Multimedia Expo (ICME)*, 2022, doi: 10.1109/ICME52920.2022.9859634.
- [41] J. Wang, X. Li, L. Hui, and J. Yang, "Stacked Conditional Generative Adversarial Networks for Jointly Learning Shadow Detection and Shadow Removal," in *Proc. IEEE/CVF Conf. Comput. Vis. Pattern Recognit. (CVPR)*, 2021.
- [42] Z. Yang, S. Ren, Z. Wu, N. Zhao, J. Wang, J. Qin, and S. He, "NPF-200: A Multi-Modal Eye Fixation Dataset and Method for Non-Photorealistic Videos," in *\*Proc. ACM Int. Conf. Multimedia (ACM MM)*, 2023.
- [43] M. Gryka, M. Terry, and G. J. Brostow, "Learning to Remove Soft Shadows," in *ACM Transactions on Graphics*, vol. XX, no. X, pp. XX-XX, 2015.
- [44] [44] L. Guo, S. Huang, D. Liu, H. Cheng, and B. Wen, "ShadowFormer: Global Context Helps Image Shadow Removal," in *\*Proc. IEEE Conf. Computer Vision and Pattern Recognition (CVPR)*, 2023.
- [45] Peter. C. Author, "Paper's name", *Proceeding of ICMLC2002 Conference*, Beijing, pp. 111-116, November 2002.
- [46] John. B. Author, and A. Friend, "Journal paper's name", *Journal's name*, Vol. 39, No. 1, pp. 222-226, Feb. 2001.
- [47] N. K. Logothetis and D. L. Sheinberg, "Visual Object Recognition," in *Annual Review of Neuroscience*, vol. 19, pp. 577-621, 1996.
- [48] S. Minaee, Y. Boykov, F. Porikli, A. Plaza, N. Kehtarnavaz, and D. Terzopoulos, "Image Segmentation Using Deep Learning: A Survey," in *Proc. IEEE Trans. Pattern Anal. Mach. Intell.*, vol. 44, no. 7, July 2022.
- [49] X. Li, C. Ma, B. Wu, Z. He, and M.-H. Yang, "Target-Aware Deep Tracking," in *Proc. IEEE/CVF Conf. Comput. Vis. Pattern Recognit. (CVPR)*, 2019, pp. 1369-1378.
- [50] M. Cordts, M. Omran, S. Ramos, T. Rehfeld, M. Enzweiler, R. Benenson, U. Franke, S. Roth, and B. Schiele, "The Cityscapes Dataset for Semantic Urban Scene Understanding," in *Proc. IEEE/CVF Conf. Comput. Vis. Pattern Recognit. (CVPR)*, 2016, pp. 3213-3223.
- [51] C. J. Willmott and K. Matsuura, "Advantages of the mean absolute error (MAE) over the root mean square error (RMSE) in assessing average model performance," *Clim. Res.*, vol. 30, pp. 79-82, 2005. DOI: 10.3354/cr030079.
- [52] U. Sara, M. Akter, M. S. Uddin, "Image Quality Assessment through FSIM, SSIM, MSE and PSNR—A Comparative Study," *Journal of Computer and Communications*, vol. 7, no. 3, March 2019, doi: 10.4236/jcc.2019.73002.